J. Fluid Mech. (2024), *vol*. 1000, A8, doi:10.1017/jfm.2024.985

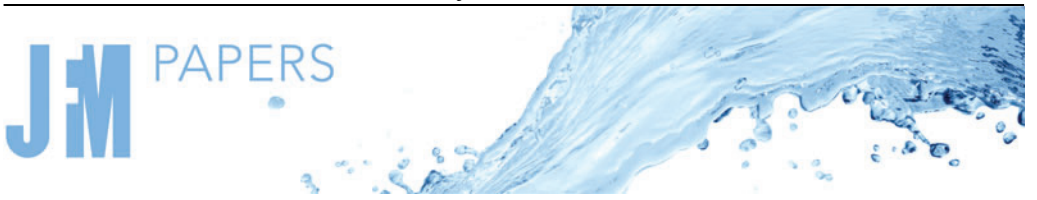

Tunable drag drop via flow-induced snap-through in origami

Rishabh Nain[1], **Tom Marzin**[1,2] **and Sophie Ramananarivo**[1,†]

[1]Laboratoire d'Hydrodynamique (LadHyX), CNRS, École polytechnique, Institut Polytechnique de Paris, 91120 Palaiseau, France

[2]Department of Chemical and Biological Engineering, Princeton University, NJ 08544, USA

(Received 27 February 2024; revised 9 August 2024; accepted 9 October 2024)

We leverage the snap-through response of a bistable origami mechanism to induce a discontinuous evolution of drag with flow speed. The transition between equilibrium states is actuated passively by airflow, and we demonstrate that large shape reconfiguration over a small increment of flow velocity leads to a pronounced and sudden drop in drag. Moreover, we show that systematically varying the geometrical and mechanical properties of the origami unit enables the tuning of this drag discontinuity and the critical speed and loading at which it occurs. Experimental results are supported by a theoretical aeroelastic model, which further guides inverse design to identify the combination of structural origami parameters for targeted drag collapse. This approach sheds light on harnessing origami-inspired mechanisms for efficient passive drag control in a fluid environment, applicable for load alleviation or situations requiring swift transitions in aerodynamic performances.

Key words: flow–structure interactions, drag reduction

1. Introduction

The drag force acting on an object typically increases with the speed of the surrounding fluid flow, as the pressure and shear stress exerted on its surface grow. For flexible bodies, this increase can be partially offset by the deformations induced by fluid forces, as it produces a more streamlined shape and reduced frontal area (Vogel 1984; Alben, Shelley & Zhang 2002; Schouveiler & Boudaoud 2006; Gosselin, de Langre & Machado-Almeida 2010; de Langre, Gutierrez & Cossé 2012; Schouveiler & Eloy 2013). This reconfiguration reduces the load compared with that of a non-deformable body; nonetheless, drag still increases monotonically with speed, although at a lower rate. However, there are a few instances where drag has been observed to drop sharply with velocity. One such

† Email address for correspondence: sophie.ramananarivo@polytechnique.edu

phenomenon occurs due to a sudden change in flow regime, referred to as drag crisis, which happens when the boundary layer transitions from laminar to turbulent, moving its separation downstream and narrowing the wake (von Wieselsberger 1921; Achenbach 1972). Another scenario involves abrupt and significant shape changes in the body, which can notably occur due to partial breakage, as observed in wind-induced tree pruning (Lopez *et al.* 2014). While this process effectively provokes a sharp decrease in the drag force and preserves the integrity of the rest of the structure, it is not reversible.

An attractive alternative is snap-through events in flexible structures, during which the elastic system undergoes a rapid transition from one equilibrium state to another. This process is swift, repeatable and produces significant shape changes, making it increasingly popular in engineering for obtaining switchable optical properties, reusable energy trapping materials, microfluidic pumps or in soft robotics (Han, Ko & Korvink 2004; Tavakol *et al.* 2014; Overvelde *et al.* 2015; Shan *et al.* 2015). Snapping instabilities occur through the application of an external input such as a point load, electrostatic forces or thermal effects, and can also be triggered by fluid flows. For example, a post-buckled sheet snaps-through and snaps-back in response to air flowing at different speeds, thus opening and closing an air inlet for flow regulation applications (Arena *et al.* 2017, 2018). The snapping of a slender membrane or arc has also been used to modify a channel resistance for passive control of viscous flow (Gomez, Moulton & Vella 2017; Peretz *et al.* 2020) or for energy harvesting from wind-induced snapping oscillations (Kim *et al.* 2020, 2021). The critical flow speed to initiate the instability can be adjusted through the nonlinear structural mechanics of the post-buckled member. Note that the system passively responds to flows, which makes it inherently autonomous and leverages the need for additional complex actuation. A few studies focused on the effect of such fast-changing geometries on aerodynamic loading. In the context of wind turbines, bistable winglets or airfoil trailing edges transition autonomously to another stable state that alleviates excessive fluid load (Arrieta *et al.* 2012; Cavens, Chopra & Arrieta 2021). While reported drag reduction is limited to about 15 % (Cavens *et al.* 2021), primarily due to a focus on lift applications, it shows potential for more substantial drag drops with appropriate designs.

A promising framework for manufacturing shape-morphing structures with nonlinear mechanical properties is the technique of origami, inspired by the Japanese art of paper folding. A surface is equipped with a set of folds, which act as a linkage mechanism, producing large three-dimensional shape changes along selected kinematic pathways that are prescribed by the folding pattern. Origami has also proven to be a powerful method to tailor targeted mechanical properties and, in particular, multistability (Li *et al.* 2019). Some specimens can thus settle in more than one stable state in the absence of external load and produce a rapid snap-through response as they pass from one equilibrium to the other (Hanna *et al.* 2014; Jianguo *et al.* 2015; Yasuda, Chen & Yang 2016; Li *et al.* 2019). It offers predictable and reversible shape transformation, with the possibility to tune the shape and number of designated stable configurations through the fold arrangement, crease torsional stiffness and assigned rest angle (Waitukaitis *et al.* 2015). Those transformable structures with programmable snap-through mechanisms have the potential to produce a controlled drop in drag at targeted flow conditions.

As a starting point, we demonstrate the potential for drag collapse with the waterbomb base, a single vertex bistable origami mechanism that is one of the fundamental origami units (Hanna *et al.* 2014; Lechenault, Thiria & Adda-Bedia 2014). This umbrella-like cell has two stable states and features a rapid snap-through response as it transitions from one to the other. Origami structures have already raised interest for drag control, due to their large morphing capabilities (Cozmei *et al.* 2020; Zhang *et al.* 2021; Marzin, de Langre & Ramananarivo 2022; Zhang, Changguo & Zhang 2022). In particular, a previous study

on the waterbomb base showed that its extreme reconfiguration tends to reduce drag to the point that it no longer increases with flow speed in the regime of large deformation (Marzin *et al.* 2022). Here, we make use of its bistable nature, which has not been utilised before for drag applications. We show that it produces a discontinuous evolution of drag with flow speed, marked by a sudden and significant drop as the structure snaps through. We systematically vary the geometrical and mechanical properties of the unit and show that it allows us to tune the drag discontinuity and the critical speed and loading at which it occurs. Experiments are captured by a simplified theoretical model that is further used for inverse design, which is finding the structural origami parameters that produce a targeted drag collapse.

2. Drag collapse through snapping

The waterbomb base consists of a disc of radius R, featuring alternating mountain and valley folds distributed evenly around a central vertex. The present study focuses on the traditional version of the origami waterbomb, comprising a total of eight folds. Additional results for different numbers of folds are presented in the supplementary material available at https://doi.org/10.1017/jfm.2024.985. The unit is rigid-foldable, meaning that facets are considered rigid, with all movement occurring at the joints, thus simplifying the kinematic analysis. In addition, we assume symmetry of motion, based on experimental observation, meaning that all the mountain folds deflect by the same amount, and the same holds for the valley folds. As a result, the mechanism reduces to a one-degree-of-freedom system (Hanna *et al.* 2014, 2015), where the shape of the entire structure can be determined from a single variable, chosen as the angle θ between a valley fold and the central axis passing through vertex (see figure 1*a*).

Importantly, this unimodal origami mechanism has two stable equilibrium states and can transition between them through snapping. When at rest, the folded unit sits in one of these stable positions with its vertex pointing in one direction (see figure 1*a* i). Upon applying an external force, the structure flattens out towards a plane that represents an unstable equilibrium. When displaced beyond this plane, it snaps through and moves to a second stable position with the vertex pointing in the opposite direction (see figure 1*a* ii). These two stable positions are characterised by angles θ_0 and θ_0^*, and although they may look similar in figure 1(*a*), they are not mirror images of each other. The relationship between the angles of mountain and valley folds, Ψ_m and Ψ_v (measured in terms of deviation to straightness, see figure 1*a*), and θ also differs on both sides of the unstable equilibrium (Hanna *et al.* 2014).

The origami bistable mechanism presents the advantage of being readily tunable. The stiffness of the folds notably influences the forces required to transition between stable states. One additional tuning parameter is the rest configuration, characterised by the angle θ_0 in the first stable state. A compact unit (with a smaller θ_0) requires more elastic energy to pass through the unstable planar state, as it has to undergo a greater deflection. The second equilibrium state θ_0^* also changes correspondingly with θ_0, modulating the amplitude of the shape change upon snapping (the relationship between θ_0 and θ_0^* is illustrated in Supplementary figure 6).

Specimens are fabricated using a technique developed in a previous study (Marzin *et al.* 2022) and inspired by the literature (Overvelde *et al.* 2016; Zuliani *et al.* 2018), which is based on layer superposition. The rigid facets are laser cut from a 350-μm-thick sheet of Mylar, which is then attached to a thinner sheet using double-sided tape, forming the creases. These folds act as elastic hinges of specific stiffness and rest angles. Rest angles are prescribed by utilising the thermoformable property of PET (see Appendix A).

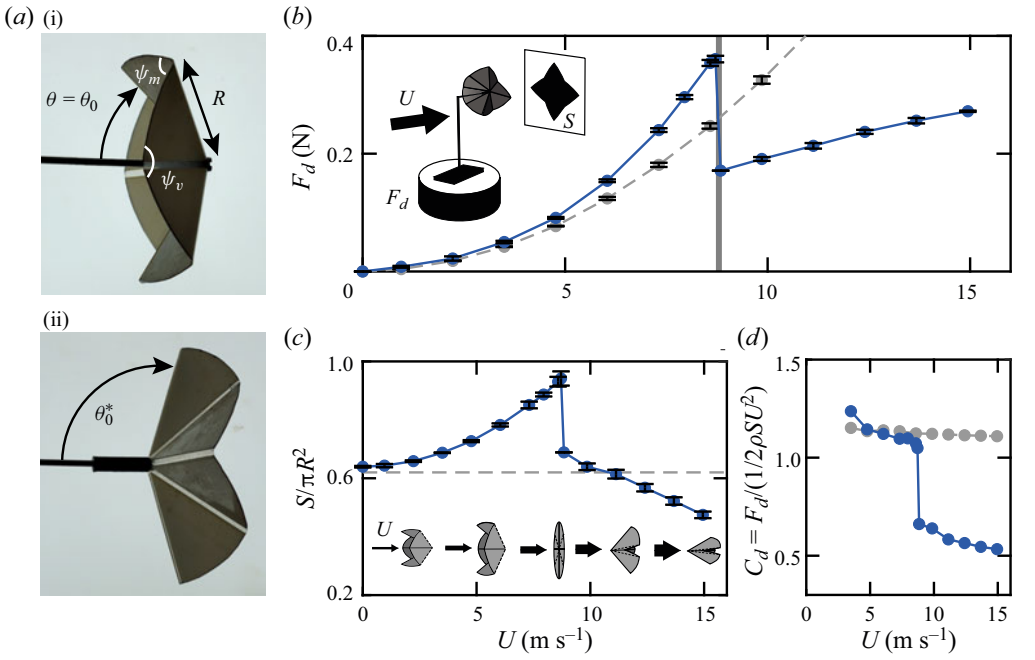

Figure 1. Drag collapse through flow-induced snap-through of a bistable origami unit. (*a*) Waterbomb base with radius R, composed of eight alternating valley and mountain folds with respective angles ψ_v and ψ_m, and with unimodal kinematics described by the angle θ. In the absence of loading, the bistable unit sits in one of two stable equilibria with angle θ_0 and θ_0^*. Evolution of (*b*) the drag force F_d in a uniform airflow with increasing velocity U, (*c*) the dimensionless frontal area $S/\pi R^2$ projected in the plane perpendicular to the flow (see schematics of the experimental set-up in the inset of *b*) and (*d*) the drag coefficient defined with respect to the instantaneous area S. The drag collapse observed in the snapping unit (with $R = 5$ cm, $\kappa = 19 \times 10^{-3}$ N and $\theta_0 = 41°$, blue solid curves) is compared with the quadratic drag of a rigid unit with the same geometry (same R and θ_0, grey dashed curves). Three tests were conducted on the same specimen, with error bars indicating the standard deviation (the grey zone denotes the variation in critical speed). Error bars for the drag coefficient are omitted for readability but are provided in the supplementary material.

As shown in a previous study, the folds then operate as torsional springs, exhibiting elastic behaviour around their assigned rest angle (Marzin *et al.* 2022). The stiffness can be adjusted by using different thicknesses of the thin sheet, ranging from 40–100 μm. To measure the stiffness experimentally, a single fold is fabricated using the same process and is tested by tracking the opening angle as an increasing torque is applied to the hinge (see Appendix A and Supplementary figure 1). The value of the stiffness is then obtained from the slope of the torque–angle curve. The fabrication process shows a standard deviation of 8% for κ.

We conducted tests on 10 origami units, sequentially varying the radius $R = 4$–7 cm, the stiffness of the folds $\kappa = 8$–92×10^{-3} N, and the rest configuration characterised by the angle $\theta_0 = 32°$–$66°$. These units are subjected to a steady air flow generated by an open jet wind tunnel with a square cross-section of width 40 cm and flow speed varied in 1–16 m s^{-1}. An elbow arm is used upstream, to hold the unit at its vertex in the centre of the cross-section (see the inset of figure 1*b*). This arm is connected to a six-component force sensor, measuring the drag component of the fluid force in the direction of the flow. For each measurement, we average the drag over 30 s and subtract the drag on the support system alone. The flow-induced shape changes are characterised

through the projected area S of the unit in the plane perpendicular to the flow, captured by a camera placed downstream and extracted through Matlab custom image analysis. The observed kinematics align with the unimodal mechanism described earlier, which is rigidly foldable with motion restricted to the joint and exhibits rotational symmetry of motion. The entire geometry of the unit can be reconstructed from S, which will be further used as the observable to measure shape reconfiguration (the relationship between S and θ is illustrated in Supplementary figure 5).

Figure 1(b) displays the evolution of drag with flow speed for a typical experiment (solid blue curve), alongside the frontal area in figure 1(c), and the drag coefficient calculated using this instantaneous area $C_d = F_d/(1/2\rho S U^2)$ in figure 1(d), to isolate the effect of shape on drag. Results are compared with the drag behaviour of a rigid cell frozen in its initial configuration (dashed grey curves), which exhibits a classical U^2 law, associated with a relatively constant drag coefficient. Initially, the unit is in its first stable position θ_0, with the concave side facing the flow. As the flow speed gradually increases, the cell symmetrically opens up, leading to a faster increase of drag compared with its rigid counterpart. This enhanced drag is attributed solely to the expansion in frontal area, as the drag coefficient actually decreases with the cell adopting a less deep, parachute-like shape, consistent with observations from simpler geometries such as hemispherical caps (Hoerner 1965; Ganedi *et al.* 2018). This drag coefficient reaches approximately $C_d = 1.1$ as the cell approaches the flat unstable state (close to the 1.17 value for a flat disc), after which the unit snaps to a more compact and streamlined configuration. Note that slight cell vibrations make it challenging to precisely attain $S/\pi R^2 = 1$. The sudden reconfiguration results in a discontinuity in the drag force on the unit, with a drop by up to 69 % among the specimens tested in this study, produced by both the significant area reduction in figure 1(c) and shape streamlining in figure 1(d). As U is further increased, the unit closes up. This closing regime has been studied extensively in a previous study (Marzin *et al.* 2022); it features an increase of drag that is slower than the quadratic U^2 law for rigid objects, owing to the reduction in frontal area exposed to the flow, combined with a decreasing drag coefficient resulting from shape streamlining.

To estimate the measurement uncertainty, we conducted three repetition of the experiments on the same specimen, re-annealed between each iteration to ensure a consistent initial configuration. Error bars in figure 1 represent the standard deviation, indicating relative variation in drag force and frontal area within 2 %. Small vibrations of the unit, especially as it approaches the unstable flat state, likely contribute to variations in the critical snapping velocity, which however remain within 2 %. Variability in the experiments were found to mainly results from the origami fabrication process. Additional tests conducted on five distinct units, all fabricated with identical parameters, exhibited a higher but reasonable dispersion, with about 10 % for the drag data, 9.5 % for the frontal area and 5 % for the critical snapping velocity (see Supplementary figure 3 and the supplementary material for more details on sources of uncertainties and measurement precision).

We thus observe a non-continuous evolution of drag with flow speed with a marked collapse. This behaviour can be described by selected observable parameters, namely the critical flow velocity of the snapping U_c, the maximum drag force reached just before snapping $F_{d,max}$ and the subsequent drag drop ΔF_d. These parameters are prominent features characterising the discontinuity but are also relevant for practical applications, such as designing protection devices or valves. They determine a maximum load, the amount of load reduction, or the critical speed at which the structure would operate. In the following section, we investigate how those quantities are related to the origami

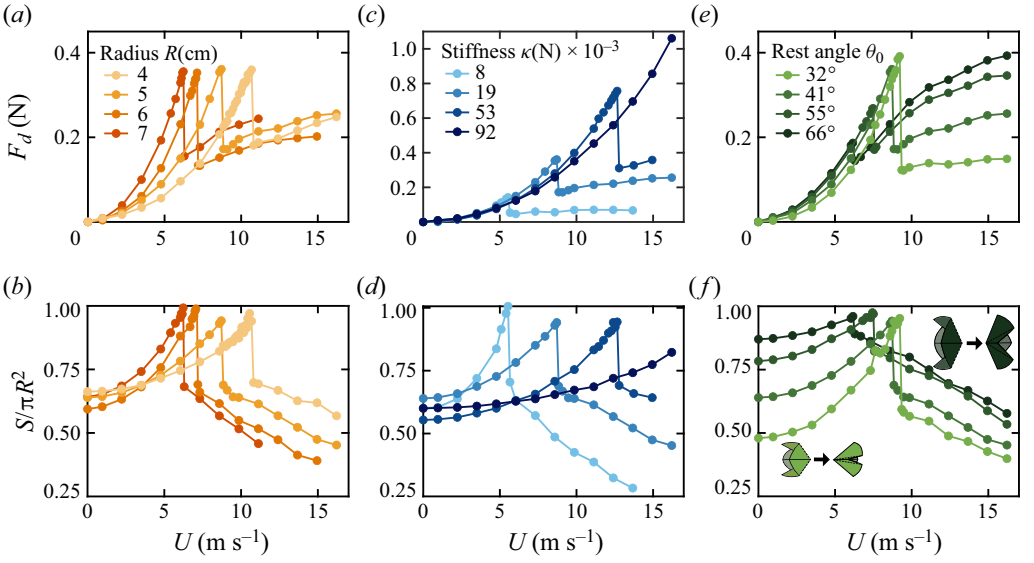

Figure 2. Influence of the origami structural parameters on drag. Evolution of (*a*,*c*,*e*) the drag force F_d and (*b*,*d*,*f*) the dimensionless frontal area $S/\pi R^2$ as a function of flow velocity U, for origami units with different (*a*,*b*) radii R, (*c*,*d*) fold stiffness κ and (*e*,*f*) rest angle θ_0. The unit $R = 5$ cm, $\kappa = 19 \times 10^{-3}$ N and $\theta_0 = 41^\circ$ is common to all graphs.

geometrical and mechanical properties, specifically its size R, rest configuration θ_0 and fold stiffness κ.

3. Aeroelastic mechanism

We first vary the radius R of the unit, while keeping the stiffness at $\kappa = 19 \times 10^{-3}$ N and the rest angle at $\theta_0 = 41^\circ$. Note that fabrication produces a small variability in the rest angle among specimens, which is visible in figure 2(*b*) in the 6 % dispersion in the dimensionless frontal area in the absence of flow ($U = 0$). As shown in figure 2(*a*,*b*), all units exhibit the characteristic behaviour described earlier, that is a non-continuous evolution of drag with flow speed with a sudden drop associated with the snap-through of the origami unit. However, bigger units (darker orange curves) initially experience a higher fluid loading, because of the larger area exposed to the flow. As a result, they reach the flat state $S/\pi R^2 = 1$ faster and flip at a lower critical speed (see figure 2*b*). Interestingly, in figure 2(*a*), the maximum drag $F_{d,max}$ experienced by the units before snapping is the same, and they feature similar jumps amplitude ΔF_d. Changing the radius of the unit thus primarily shifts the critical velocity U_c at which the drag collapse occurs, while preserving $F_{d,max}$ and ΔF_d.

Figure 2(*c*,*d*) shows the results for origami cells with different fold stiffness, but the same size $R = 5$ cm and rest angle $\theta_0 = 41^\circ$ (with a similar degree of variability as earlier). Stiffer units (darker blue curves) deploy slower with increasing U owing to larger resistance to deformation, and reach the flat state at larger critical velocities (see figure 2*d*). The most rigid one does not reach this unstable point within the range of flow covered here. Snapping at larger speeds U_c results both in higher drag peak values $F_{d,max}$ and larger jumps ΔF_d (see figure 2*c*). Stiffness thus affects all three drag features, offering an additional lever for control.

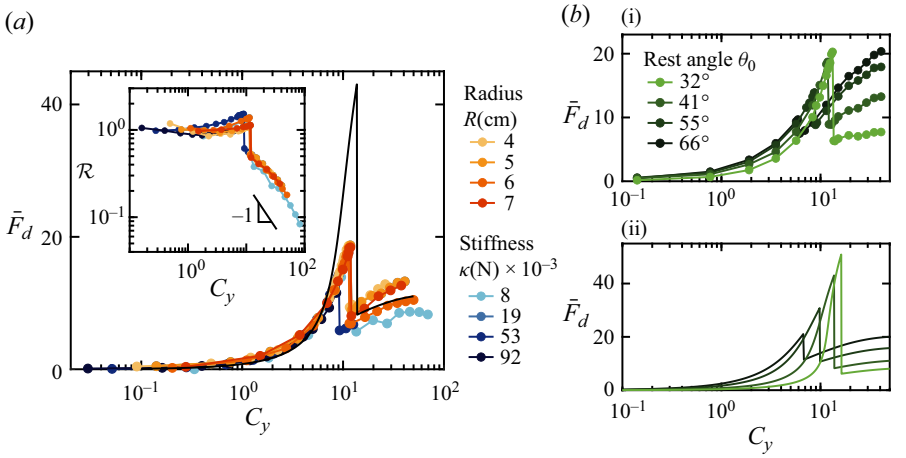

Figure 3. Aeroelastic mechanism. (*a*) Evolution of the dimensionless drag $\overline{F_d} = F_d/\kappa$ as a function of the Cauchy number $C_y = \rho U^2 R^2/\kappa$ for origami units with different radii R and fold stiffness κ (with the same rest angle $\theta_0 = 41°$). The inset shows the reconfiguration number $\mathcal{R} = F_d/F_{d,r}$, which compares the drag force F_d with that of a rigid unit having the same geometry $F_{d,r}$. (*b*) Plot of $\overline{F_d}$ as a function of C_y for units with different initial degree of opening θ_0 (with the same $R = 5$ cm and $\kappa = 19 \times 10^{-3}$ N). Experimental force data are compared with theoretical predictions (solid curves).

Finally, we vary the degree of opening of the cell rest state θ_0, while keeping the size and stiffness constant as $R = 5$ cm and $\kappa = 19 \times 10^{-3}$ N, respectively. Starting from a more compact rest state (lighter green curves) delays the flipping towards higher flow velocities, as depicted in figure 2(*f*). Intuitively, reaching the flat state that is further away requires greater work from fluid loading. As was the case for the κ-series of units, snapping at greater U_c results in larger maximal drag $F_{d,max}$ in figure 2(*e*). As mentioned earlier and illustrated in the schematics of figure 2(*f*), changing θ_0 also affects the degree of closure of the second stable state. Small θ_0 (light green) results in a larger collapse in the frontal area post-snapping compared with units initially more opened (dark green) in figure 2(*f*). It correspondingly leads to larger jumps in drag ΔF_d in figure 2(*e*). The rest angle thus completes the set of three parameters that will allow us to adjust the three drag characteristics U_c, $F_{d,max}$ and ΔF_d.

The trends observed through variations in parameters reflect the interplay between external fluid loading and elastic restoring forces of the origami unit, which governs the unit's reconfiguration process. This fluid–elastic competition can be analysed in terms of Cauchy number C_y, as introduced in a previous study (Marzin *et al.* 2022) and frequently used in the literature (Alben *et al.* 2002; Gosselin *et al.* 2010; de Langre *et al.* 2012). This dimensionless number examines the relative magnitudes of the work done by fluid forces, $\rho U^2 R^3$, and the elastic energy of folding, κR:

$$C_y = \frac{\rho U^2 R^2}{\kappa}. \tag{3.1}$$

In figure 3(*a*), drag measurements are re-plotted in the dimensionless form $\overline{F_d} = F_d/\kappa$ as a function of C_y, using the fold stiffness κ as a characteristic force scale, in line with Marzin *et al.* (2022). Here, we only report data for units with different stiffness κ and radius R, which share the same initial rest configuration θ_0. Data collapse onto a master curve, with a drag peak and subsequent jump that are solely set by the fold stiffness, and which occur at a critical Cauchy number of $C_{y,c} \approx 14$ for all units. Alternatively, the

reconfiguration number $\mathcal{R} = F_d/F_{d,r}$ is often used to discuss the effect of deformability on drag (Schouveiler & Boudaoud 2006; Gosselin *et al.* 2010). It compares the drag force F_d on the deforming cell to that on a rigid unit with the same geometry $F_{d,r}$, which is evaluated by fitting a U^2 law to drag measurements at low speeds where deformation is minimal. The curve of $\mathcal{R}$ as a function of C_y in figure 3(*a*) highlights distinct drag scaling regimes. At low C_y, where fluid loading is small compared with structural rigidity, the drag behaves like that of a rigid body, and $\mathcal{R} \sim 1$. As C_y increases, $\mathcal{R}$ rises due to the larger frontal area of the cell, then drops sharply below 1 at the critical Cauchy number $C_{y,c}$, and continues to decrease continuously with further deformation. In the large-deformation regime, $\mathcal{R}$ declines with a logarithmic slope approaching -1, consistent with the plateau-like behaviour for drag observed in a previous study on the waterbomb unit (Marzin *et al.* 2022). We previously showed that the dimensionless quantities C_y and $\overline{F_d}$ capture the effect of origami size and stiffness in fluid–elastic mechanisms. However, it does not account for the more intricate influence of the rest angle θ_0. As shown in figure 3(*b* i), the latter affects the peak and jump value of $\overline{F_d}$, as well as the critical Cauchy number for snapping.

Next, we develop a simplified theoretical model to further explore and corroborate the link between the origami unit's characteristics and drag. This model will also be used for the inverse problem. It employs the same energy approach as previous work on the closing dynamics of the waterbomb unit in a flow (Marzin *et al.* 2022) and has been extended to account for the snapping. We provide a brief overview of the main elements of the model here, and additional details can be found in Appendix A and in Marzin *et al.* (2022). The static equilibrium of the unit in a flow is determined through the minimisation of its energy $E_{el} - W$, comprising both the elastic potential energy associated with folding E_{el} and the work done by fluid forces W as the unit deforms:

$$E_{el} - W = 4\frac{\kappa R}{2}[(\psi_m - \psi_m^0)^2 + (\psi_v - \psi_v^0)^2] - 8\int_{\theta_0}^{\theta}\int_{S_f} \rho(\boldsymbol{U}\cdot\boldsymbol{n}_{\theta'})^2\,\mathrm{d}S_f\boldsymbol{n}_{\theta'}\cdot\mathrm{d}\boldsymbol{X}_{\theta'}, \tag{3.2}$$

where ρ is the air density and $S_f = \pi R^2/8$ is the facet area (with other quantities introduced subsequently). The first term of (3.2) corresponds to the elastic potential energy of the four mountain and four valley folds, modelled as elastic torsional springs with stiffness κ. It scales with the square of the deviation of their respective angles ψ_m and ψ_v to their rest values ψ_m^0 and ψ_v^0 (Hanna *et al.* 2014). The second term corresponds to the work done by fluid forces acting on the unit facets, which is the same for all eight facets owing to the rotational symmetry of motion. The Reynolds number for our experiments falls within the range $Re = UR/\nu \approx 10^3$–10^5, where form drag predominates over friction drag, and the latter is neglected. As discussed in Marzin *et al.* (2022), friction forces likely become significant in regimes with substantial deformation, where facets nearly align with the flow. However, this particular regime is not reached in our present study. Consistent with earlier studies on the reconfiguration of flexible structures in a flow (Schouveiler & Boudaoud 2006; Gosselin *et al.* 2010; Schouveiler & Eloy 2013; Marzin *et al.* 2022), pressure is computed using conservation of momentum principles. It is proportional to the square of the component of flow momentum perpendicular to the facet, denoted as $\rho(\boldsymbol{U}\cdot\boldsymbol{n}_\theta)^2$, where $\boldsymbol{n}_\theta$ represents the normal unit vector. While simplified, this model has demonstrated effectiveness in capturing fluid–elastic behaviours (Schouveiler & Boudaoud 2006; Gosselin *et al.* 2010; Schouveiler & Eloy 2013; Marzin *et al.* 2022). It offers a reasonable approximation of more complex potential flow expressions (Alben, Shelley & Zhang 2004; Marzin *et al.* 2022), which would be challenging to implement

for three-dimensional geometries. The pressure force is integrated over the facet area S_f and its work is computed along the facet trajectory, with $d\boldsymbol{X}_\theta$ the local displacement. By expressing the energy in a dimensionless form as $\overline{E_{el}-W} = (E_{el}-W)/\kappa R$, the previously introduced Cauchy number C_y emerges as the pertinent fluid–elastic parameter:

$$\overline{E_{el}-W} = 2\big[(\psi_m-\psi_m^0)^2+(\psi_v-\psi_v^0)^2\big] - 8C_y\int_{\theta_0}^{\theta}\int_{\bar{S}_f}\rho(\boldsymbol{e}_z\cdot\boldsymbol{n}_{\theta'})^2\,\mathrm{d}\bar{S}_f\boldsymbol{n}_{\theta'}\cdot\mathrm{d}\bar{\boldsymbol{X}}_{\theta'}, \tag{3.3}$$

where $\bar{\cdot}$ denotes dimensionless quantities, using the radius as characteristic length, and $\boldsymbol{e}_z$ is the unit vector in the direction of the flow. In (3.3), all kinematic variables of the one-degree-of-freedom mechanism depend on a single parameter θ. However, these relationships differ on each side of the flat state. The equilibrium angle θ, which satisfies $\mathrm{d}(\overline{E_{el}-W})/\mathrm{d}\theta = 0$, is determined numerically while gradually increasing the Cauchy number, first addressing the opening phase of the kinematics. As the system approaches the flat state at $\theta = 90^\circ$ beyond a specific criterion, the kinematic relations are modified to describe the closing phase. From the static equilibrium angle θ, we can determine the drag force acting on the unit as the component of fluid pressure forces in the direction of the flow (see Appendix A).

Theoretical drag results are presented in figure 3(*a*) in dimensionless form, considering a given rest angle $\theta_0 = 41^\circ$ based on experiments (black solid line). The simplified model successfully captures experimental features, displaying a peak in drag that remains unaffected by the unit's size, followed by a sudden drop at a critical Cauchy number. Although the model tends to overestimate $F_{d,max}$ and ΔF_d, the quantitative agreement is reasonable, considering that no adjustable parameters were used and the simplifications made. As depicted in figure 3(*b* ii), the model also effectively captures the effect of varying the initial rest angle θ_0 on drag. A more compact unit exhibits a higher drag peak and jump, along with a higher critical Cauchy number. This model will be valuable for the inverse design of origami units to achieve the desired drag, as we discuss in the next section.

4. Inverse design approach

We have characterised how the waterbomb unit features influence its drag behaviour. We now pose the question: 'Can we identify the specific geometrical and mechanical origami parameters that would lead to a targeted drag collapse in a uniform fluid flow?'. More specifically, we formulate the inverse problem where the objective is to find the optimal set of parameters (R, κ, θ_0) that will result in a collapse of drag, with a predefined target peak drag force $F^t_{d,max}$ and jump ΔF^t_d value at a critical flow speed U^t_c. To address this, we use the model presented earlier and validated experimentally, which establishes a relationship between the parameters (R, κ, θ_0) and the resulting drag characteristics $(F_{d,max}, \Delta F_d, U_c)$. The optimisation is implemented numerically in Matlab using the *trust-region-dogleg* algorithm of *fsolve* solver. It solves the system of equations $F_d - F^t_{d,max} = 0$, $\Delta F_d - \Delta F^t_d = 0$ and $U_c - U^t_c = 0$ with respect to the origami unit's features (R, κ, θ_0). The algorithm finds a single solution, satisfying the constraints by a maximum residual of $O(10^{-19})$ within a hundred iterations.

To validate the inverse design approach, we test our prediction experimentally by fabricating the optimised design and measuring the evolution of its drag with flow speed. While the specific radius R and rest angle θ_0 can be easily implemented through laser-cutting and an adjustable mount, achieving an arbitrary fold stiffness κ is more challenging. This limitation arises from the finite number of sheet thicknesses available for

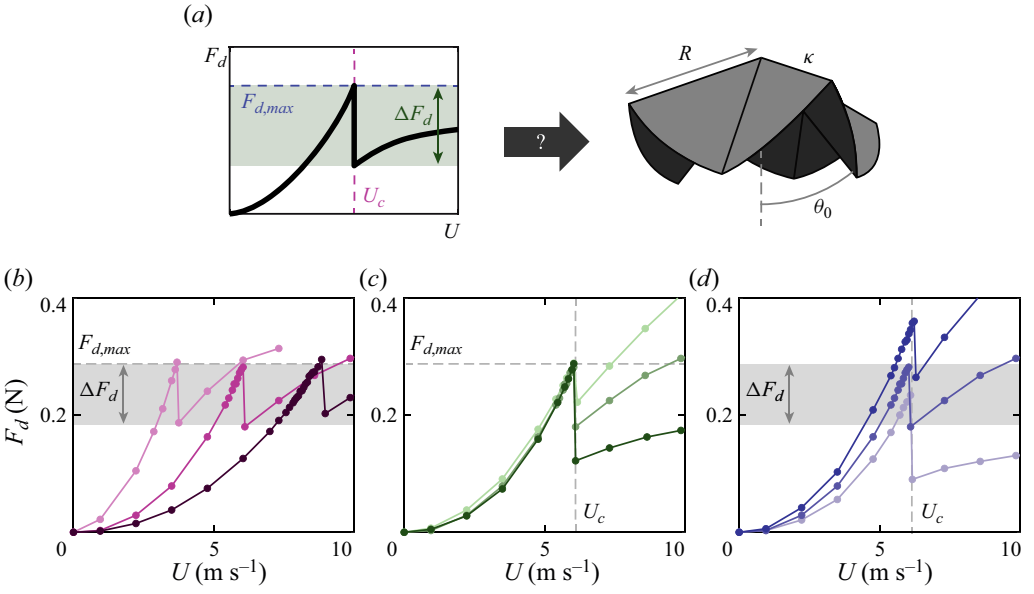

Figure 4. Targeting drag collapse features. (*a*) The inverse design approach consists of finding the set of origami structural parameters (R, κ, θ_0) that will lead to a collapse of drag with a targeted maximum before snapping $F_{d,max}$, jump ΔF_d and occurring at a defined critical flow speed U_c. Evolution of drag with flow speed for physical prototypes of optimised origami designs, which are calculated to produce a selective variation of (*b*) U_c, (*c*) ΔF_d and (*d*) $F_{d,max}$, while keeping the two remaining features identical. Respective target values of (U_c, ΔF_d, $F_{d,max}$) are indicated in Appendix A.

manufacturing the folds. To overcome this constraint, we introduce slits in the folds. These slits modulate the effective length of the folds and, consequently, their stiffness, enabling a controlled variation of κ by adjusting their number (see Appendix A and Supplementary figure 2).

To demonstrate our ability to control the drag behaviour, we create sets of specimens with one parameter gradually changing while keeping the other two fixed. We first vary the targeted critical flow speed for snapping, as $U_c^t = [4, 7, 10]$ m s^{-1}, while prescribing constant peak drag value $F_{d,max}^t = 0.8$ N and jump $\Delta F_d^t = 0.6$ N. The corresponding optimised origami parameters (R, κ, θ_0) are provided in Appendix A. Consistent with the differences observed earlier in figure 3 between experiments and theory, the experimental realisations exhibit lower values in figure 4(*b*), namely $U_c = [3.7, 6.0, 8.8]$ m s^{-1}, $F_{d,max} = 0.29$ N and $\Delta F_d = 0.10$ N. Nevertheless, we successfully achieved a gradual variation in U_c while keeping the other two parameters unchanged. Note that the optimised designs have the same rest angle and fold stiffness, but varying radius, which is consistent with the previous results shown in figure 2(*a*). We indeed demonstrated that $F_{d,max}$ and ΔF_d are size-independent and, therefore, determined by the specific combination of (κ, θ_0). In figure 4(*c*,*d*), we systematically vary the jump ΔF_d and peak $F_{d,max}$, respectively (target values are reported in Appendix A). Similarly, although the physical samples have drag quantities below the target values, they still showcased the intended selective variations. Our results confirm the validity of our inverse design approach, but there are limitations to how closely we can match desired drag behaviours. These limitations arise primarily from the theoretical model employed in the optimisation procedure. While it accurately captures the effect of origami parameters on drag, it only provides semi-quantitative agreement with the experimental data. Note that deviations

between the targeted drag features and those of the resulting optimised design in figure 4 align with differences reported in prior experimental–theoretical comparisons of figure 3 (see Supplementary figures 11 and 12). Refining the model, notably using a more realistic representation for the fluid dynamics, is thus expected to produce better quantitative results.

5. Conclusion and discussion

In this study, we leverage the waterbomb base's bistability to sharply reduce drag force with flow velocity. A uniform airflow unfolds the origami unit, which, upon reaching a flat state, undergoes a snap-through to a more streamlined shape, causing a sudden collapse of drag. While the use of elastic deformation to mitigate drag increase with flow speed is not novel (Vogel 1984; Alben *et al.* 2002; Schouveiler & Boudaoud 2006; Gosselin *et al.* 2010; de Langre *et al.* 2012; Schouveiler & Eloy 2013); here, a decrease is achieved through significant and abrupt shape changes over a small increment of fluid input load. Importantly, the snap-through is tunable based on the cell radius, fold stiffness and rest angle, providing control over drag characteristics.

We show that the cell behaviour results from the quasi-static mechanical equilibrium between actuating fluid loading and restoring elastic forces, captured by a Cauchy number. The snap-through occurs at a fixed critical Cauchy number for a given cell rest angle. The later serves as an additional control, influencing both snap-through onset and drag changes. These experimental features are captured by a theoretical fluid–elastic model, portraying the cell as rigid facets with folds acting as elastic hinges, and utilising an empirical formulation for fluid pressure forces, consistent with prior studies. The model effectively accounts for the influence of cell structural parameters on drag, demonstrating reasonable predictiveness despite a tendency to overestimate drag. However, such discrepancies are expected due to the absence of adjustable parameters and the simplified representation of the origami's elastic response and fluid dynamics. Force-deflection tests on the waterbomb unit show reasonable agreement with the idealised mechanical model, though some softening near the flat state is observed, possibly due to vertex effects or fabrication imperfections (see Supplementary figure 8). A modified model, using elastic potential energy derived from these tests, suggests that this softening might cause snap-through at a lower critical speed and a reduced peak drag. Nevertheless, it only marginally accounts for the discrepancies between the theoretical predictions and the experimental results shown in figure 3(*a*). These differences likely arise from the simplified description of fluid dynamics, which notably does not account for the object's feedback on the flow. Local fluid forces, which are not influenced by the object's overall shape or wake, result in a drag coefficient of $C_d = 2$ when the unit reaches the flat state, where drag is typically overestimated, compared with the expected value of 1.17 for a disc. To address this, we can introduce a corrective pressure coefficient C, such that $P = C\rho(\boldsymbol{U} \cdot \boldsymbol{n_\theta})^2$, to align the drag coefficient to that of a disc in the flat configuration. This adjustment changes the critical Cauchy number for snapping, but it does not resolve the peak drag overestimation. Further improvements could involve using a variable pressure coefficient or a more refined spatial pressure force distribution that adapts to the cell reconfiguration. Flow visualisation or computational fluid dynamics simulations would then be instrumental in determining the shape dependence of this pressure field and improving the predictive accuracy of the model.

The modelling framework provides the system equations to guide inverse design, intending to identify the combination of structural parameters leading to a targeted

drag collapse. Our implementation showcases an advanced level of control, allowing selective adjustment of key drag features: namely, the peak drag before snapping, the drag drop and the critical flow speed at which it occurs. Although the number of folds is not included in our current inverse design framework, it has a distinctive effect on drag (see supplementary material). It could be a valuable parameter for expanding the design space and controlling additional drag characteristics, such as the rate at which drag increases again after dropping. Currently, quantitative predictability is contingent on the model's accuracy and the precise control of the origami's mechanical properties during fabrication. Improved closeness to the target is anticipated with more refined fluid–elastic models and advancements in manufacturing techniques, positioning this work as promising proof of concept. It illustrates the potential of origami as a platform for programming drag-vs-speed behaviour.

This programmability holds value for self-protection strategies, mitigating excessive aerodynamic loads beyond a predetermined threshold. Force transitions above a tunable critical flow velocity could also serve as a velocity threshold detector. The switch-like response of the waterbomb base also holds the potential for fluidic control in a channel, for example, acting as a relief valve. It would obstruct a conduct as it deploys and discharges the fluid beyond a predetermined pressure level, limiting pressure built up. For the waterbomb base, snap-through involves passing through an unstable flat state, leading to an initial drag increase greater than that of a rigid object. This enhanced drag could be advantageous for stabilisation or speed-reduction in applications such as sea anchors, drogues or stabilisers for aerial refuelling pipes (Holler 1985; Wei *et al.* 2016). Such shape-adaptive drag may offer better control and stabilisation compared with fixed-shape designs in varying fluid environments. However, drag enhancement is not a universal feature of bistable origami mechanisms, as some do not require transitioning through a flat state (Waitukaitis *et al.* 2015). Rapid morphing can also result from torsional instabilities caused by axial asymmetry in the folds, though this was not observed in this study. In addition, 'hidden' degrees of freedom not explicit in the crease pattern, such as facet bending (Liu & Felton 2018), could enable substantial shape changes while maintaining minimal deformation and a relatively constant drag coefficient before snap-through.

Here, morphing is driven aeroelastically, enabling the component to autonomously respond to the local environment, and eliminating the need for additional sensing and control systems. Such passive mechanisms allow for a more streamlined structural design of the aerodynamic control surface. However, a bistable mechanism requires external intervention or a counter-flow to return to its original state. This ability to retain the inverted state could be advantageous for functioning as a memory unit, storing information about past fluid conditions, similar to (Jules *et al.* 2022). Alternatively, using a monostable system that snaps through when loaded but returns to its original state when the load is removed could address this limitation (Arena *et al.* 2017; Gomez *et al.* 2017; Arena *et al.* 2018). This could be achieved with restoring springs that pull the unit back to its original position when the airspeed decreases. Further study is needed to assess the multistability of such systems and to identify configurations where they are bistable, monostable with snap-through or stable without snap-through.

Another advantage of origami is the ability to easily combine multiple bistable elements to produce multistable structures (Silverberg *et al.* 2014; Li & Wang 2015; Sengupta & Li 2018; Jules *et al.* 2022). An example is shown in figure 5, featuring a chain made of two waterbomb cells with the same size and different rest angle and fold stiffness (see also Supplementary figure 9). It produces two successive sharp transitions in the drag force. With sufficient spatial separation, each unit is expected to have its independent flow

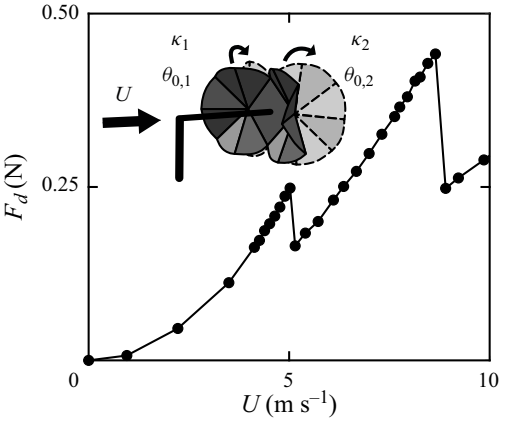

Figure 5. Leveraging multistability for a double drag collapse. A multistable origami structure is formed through the assembly of two waterbomb units, with different fold stiffness $\kappa_1 = 19 \times 10^{-3}$ N and $\kappa_2 = 53 \times 10^{-3}$ N and rest angle $\theta_{0,1} = 56^\circ$ and $\theta_{0,2} = 71^\circ$, and the same radius $R = 5$ cm (inset). The successive snap-throughs lead to sequential drag collapses when exposed to a uniform flow with increasing speed.

velocity threshold initiating snap-through. Other configurations might, however, lead to interactions between cells through external flow, resulting in a more complex collective response, as observed in fluidic cellular origami (albeit for internal pressurisation) (Li & Wang 2015). Alternatively, if cells share facets, they can also communicate the mechanical state of one unit to its neighbour, forming logic elements (Treml *et al.* 2018). This has the potential to generate more complex snapping sequences and subsequent drag evolution with flow speed for advanced adaptive functionalities.

Supplementary material. Supplementary material is available at https://doi.org/10.1017/jfm.2024.985.

Funding. We acknowledge support from a JCJC grant of the Agence Nationale de la Recherche (ANR-20-CE30-0009-01) to S.R. and from the Agence Innovation Défense to T.M.

Data availability statement. The datasets generated during the current study are available from the corresponding author upon request.

Declaration of interests. The authors report no conflict of interest.

Author ORCID.
Rishabh Nain https://orcid.org/0009-0000-0156-2302;
Tom Marzin https://orcid.org/0000-0002-7465-1792;
Sophie Ramananarivo https://orcid.org/0000-0003-1049-4131.

Appendix A

A.1. *Origami fabrication*

Specimens are fabricated using a layer superposition method. The rigid facets are laser cut from a 350-μm-thick sheet of Mylar, which is then attached to a thinner sheet using double-sided tape with a 2.5 mm spacing that forms the creases. The folded unit is then maintained in a desired configuration on a mount, placed in a heating chamber for an hour at 75 °C, and then left to cool down at room temperature. It thus effectively prescribes the first stable state θ_0. This annealing process relaxes any residual stresses that might have been created during folding (Lechenault *et al.* 2014) so that the first stable state is close to a zero-energy state.

Sheet thickness (μm)	48	50	75	100
Fold stiffness κ(N) $\times 10^{-3}$	8	19	53	92

Table 1. Stiffness measured for folds made from sheets with different thickness.

A.2. *Fold stiffness*

To measure fold stiffness, a prototype of a single crease was designed using the manufacturing process outlined in § A.1 and in Marzin *et al.* (2022). While keeping one of the facets fixed vertically, we apply a variable increasing point load to the geometrical centre of the free facet and extract the opening angle of the fold Ψ (see Supplementary figure 1*a*). The opening angle in the absence of load is set to $\Psi_0 \approx 113^\circ \pm 8^\circ$ for all the tests, but note that the stiffness was found independent of Ψ_0 in the previous study of Marzin *et al.* (2022). The fold acts as a torsional spring, exhibiting a linear relationship between the torque applied T (accounting for the weight of the hanging facet as well) and the angular deviation $\Psi - \Psi_0$ (see Supplementary figure 1*b*). The stiffness is extracted from the slope as $T = \kappa L(\Psi - \Psi_0)$, with $L = 4$ cm the crease length. Table 1 lists κ values for the four thin sheets. Repeatability and robustness were assessed by measuring κ for eight folds from a 50 μm sheet, resulting in an 8 % variability based on standard deviation relative to the mean value.

To expand the range of achievable stiffness values, we employ a strategy inspired by prior work (Zuliani *et al.* 2018) and introduce slits in the folds. Slits with 5 mm length are evenly distributed along the crease length, and span its width (see Supplementary figure 2*a*). Adjusting their number modulates the effective length of the fold, thereby changing its stiffness and facilitating the attainment of diverse κ values. As shown in Supplementary figure 2(*b*), the stiffness of a slitted fold scales linearly with its effective length, with a 7 % deviation from the expected linear relationship. To ensure that the presence of slits has minimal effect on the interaction of the origami unit with the flow, we conducted experiments with two specimens, one with slitted folds and another with unslitted folds, both having the same stiffness. These two specimens exhibited identical drag curves, indicating that the slits did not significantly affect the performance in the flow (see Supplementary figure 2).

A.3. *Fluid–elastic model*

The equilibrium angle θ of the unit in the flow is given by the zeros of $\mathrm{d}\overline{(E_{el} - W)}/\mathrm{d}\theta$, with $\overline{E_{el} - W}$ expressed in (3.3). As further detailed in the supplementary material, it yields the equation

$$(\psi_m - \psi_m^0)\frac{\mathrm{d}\psi_m}{\mathrm{d}\theta} + (\psi_v - \psi_v^0)\frac{\mathrm{d}\psi_v}{\mathrm{d}\theta} + \frac{2}{3}C_y \sin^2\theta \sin^2\phi \left[A\frac{\mathrm{d}\phi}{\mathrm{d}\theta}\sin\theta + B\sin\phi\right] = 0, \tag{A1}$$

where $C_y = \rho U^2 R^2/\kappa$ is the same Cauchy number as defined for experiments, ϕ is the angle between valley folds and the central axis, and A and B are constants. Assuming rigid folding and symmetry of motion, the expression for all angles in (A1) can be derived as a

Target values			Cell parameters		
$F^t_{d,max}$ (N)	U^t_c (m s^{-1})	ΔF^t_d (N)	κ (N) $\times 10^{-3}$	R (cm)	θ_0 (deg.)
0.8	4	0.6	21	4.6	47
0.8	7	0.6	21	6.5	47
0.8	10	0.6	21	11.4	47
0.8	7	0.5	27	6.5	56
0.8	7	0.7	16	6.5	33
0.65	7	0.6	11	5.9	25
0.95	7	0.6	32	7.1	56

Table 2. Fabrication parameters produced by the optimisation algorithm, for given target drag parameters.

function on θ (see Brunck *et al.* 2016; Marzin *et al.* 2022 and the supplementary material):

$$\phi(\theta) = \begin{cases} \arccos\left(\dfrac{\cos\alpha\cos\theta}{1+\sin\alpha\sin\theta}\right), & \text{for } 0 \le \theta \le \pi/2, \\ \arccos\left(\dfrac{\cos\alpha\cos\theta}{1-\sin\alpha\sin\theta}\right), & \text{for } \pi/2 < \theta \le \pi-\alpha, \end{cases} \tag{A2}$$

with $\alpha = 2\pi/8$ the sector angle of a facet. Angles of the mountain and valley folds are given by $\cos\psi_v = \cos 2\theta$ and $\cos\psi_m = \cos 2\phi$. Note that the expressions as a function of θ differ on each side of the flat configuration $\theta = \pi/2$, describing, respectively, the opening and closing kinematics.

Equation (A1) is numerically solved using the nonlinear system solver *fsolve* of Matlab. The Cauchy number is varied linearly from 0 to 50 in 500 steps, and the solver utilises the value of θ obtained at the previous iteration as a starting point (initialising at θ_0 for $C_y = 0$). As θ approaches the flat state beyond $\pi/2 - \epsilon$, with $\epsilon = 0.01$ rad, (A1) is then solved using the new set of angle expressions describing the closing kinematics, with the first starting point at $\pi/2 + \epsilon$.

From the equilibrium angle θ, we obtain the dimensionless projected surface $S/\pi R^2 = \sin\theta\sin\phi$, the dimensionless drag force $\overline{F_d} = \pi C_y \sin^3\theta \sin^3\phi$ (by projecting fluid pressure forces in the direction of the flow), for comparison with experimental results (see the supplementary material for more details).

A.4. *Inverse design*

The target values ($F^t_{d,max}$, ΔF^t_d, U^t_c) used, along with the corresponding cell parameters, are presented in table 2. When varying U_c (while keeping the other two drag features constant), cells with the same radius but different κ and θ_0 are obtained. Interestingly, selectively varying ΔF_d is achieved by adjusting θ_0 and κ while maintaining a constant R.

References

ACHENBACH, E. 1972 Experiments on the flow past spheres at very high Reynolds numbers. *J. Fluid Mech.* **54** (3), 565–575.

ALBEN, S., SHELLEY, M. & ZHANG, J. 2002 Drag reduction through self-similar bending of a flexible body. *Nature* **420** (6915), 479–481.

ALBEN, S., SHELLEY, M. & ZHANG, J. 2004 How flexibility induces streamlining in a two-dimensional flow. *Phys. Fluids* **16** (5), 1694–1713.

ARENA, G., GROH, R.M.J., BRINKMEYER, A., THEUNISSEN, R., WEAVER, P.M. & PIRRERA, A. 2017 Adaptive compliant structures for flow regulation. *Proc. R. Soc.* A **473** (2204), 20170334.

ARENA, G., GROH, R.M.J., THEUNISSEN, R., WEAVER, P.M. & PIRRERA, A. 2018 Design and testing of a passively adaptive inlet. *Smart Mater. Struct.* **27** (8), 085019.

ARRIETA, A.F., BILGEN, O., FRISWELL, M.I. & HAGEDORN, P. 2012 Passive load alleviation bi-stable morphing concept. *AIP Adv.* **2** (3), 032118.

BRUNCK, V., LECHENAULT, F., REID, A. & ADDA-BEDIA, M. 2016 Elastic theory of origami-based metamaterials. *Phys. Rev.* E **93** (3), 033005.

CAVENS, W.D.K., CHOPRA, A. & ARRIETA, A.F. 2021 Passive load alleviation on wind turbine blades from aeroelastically driven selectively compliant morphing. *Wind Energy* **24** (1), 24–38.

COZMEI, M., HASSELER, T., KINYON, E., WALLACE, R., DELEO, A.A. & SALVIATO, M. 2020 Aerogami: composite origami structures as active aerodynamic control. *Compos.* B **184**, 107719.

GANEDI, L., OZA, A.U., SHELLEY, M. & RISTROPH, L. 2018 Equilibrium shapes and their stability for liquid films in fast flows. *Phys. Rev. Lett.* **121** (9), 094501.

GOMEZ, M., MOULTON, D.E. & VELLA, D. 2017 Passive control of viscous flow via elastic snap-through. *Phys. Rev. Lett.* **119** (14), 144502.

GOSSELIN, F., DE LANGRE, E. & MACHADO-ALMEIDA, B.A. 2010 Drag reduction of flexible plates by reconfiguration. *J. Fluid Mech.* **650**, 319.

HAN, J.S., KO, J.S. & KORVINK, J.G. 2004 Structural optimization of a large-displacement electromagnetic lorentz force microactuator for optical switching applications. *J. Micromech. Microengng* **14** (11), 1585.

HANNA, B.H., LUND, J.M., LANG, R.J., MAGLEBY, S.P. & HOWELL, L.L. 2014 Waterbomb base: a symmetric single-vertex bistable origami mechanism. *Smart Mater. Struct.* **23** (9), 094009.

HANNA, B.H., MAGLEBY, S.P., LANG, R.J. & HOWELL, L.L. 2015 Force–deflection modeling for generalized origami waterbomb-base mechanisms. *J. Appl. Mech.* **82** (8), 081001.

HOERNER, S.F. 1965 Fluid-dynamic drag. *Hoerner fluid dynamics*. Available at https://ia600707.us.archive.org/13/items/FluidDynamicDragHoerner1965/Fluid-dynamic_drag__Hoerner__1965_text.pdf.

HOLLER, R. 1985 Hydrodynamic drag of drogues and sea anchors for drift control of freefloating buoys. In *OCEANS'85-Ocean Engineering and the Environment*, pp. 1330–1335. IEEE.

JIANGUO, C., XIAOWEI, D., YA, Z., JIAN, F. & YONGMING, T. 2015 Bistable behavior of the cylindrical origami structure with Kresling pattern. *J. Mech. Des.* **137** (6), 061406.

JULES, T., REID, A., DANIELS, K.E., MUNGAN, M. & LECHENAULT, F. 2022 Delicate memory structure of origami switches. *Phys. Rev. Res.* **4** (1), 013128.

KIM, H., LAHOOTI, M., KIM, J. & KIM, D. 2021 Flow-induced periodic snap-through dynamics. *J. Fluid Mech.* **913**, A52.

KIM, H., ZHOU, Q., KIM, D. & OH, I.-K. 2020 Flow-induced snap-through triboelectric nanogenerator. *Nano Energy* **68**, 104379.

DE LANGRE, E., GUTIERREZ, A. & COSSÉ, J. 2012 On the scaling of drag reduction by reconfiguration in plants. *C. R. Méc.* **340** (1–2), 35–40.

LECHENAULT, F., THIRIA, B. & ADDA-BEDIA, M. 2014 Mechanical response of a creased sheet. *Phys. Rev. Lett.* **112** (24), 244301.

LI, S., FANG, H., SADEGHI, S., BHOVAD, P. & WANG, K.-W. 2019 Architected origami materials: how folding creates sophisticated mechanical properties. *Adv. Mater.* **31** (5), 1805282.

LI, S. & WANG, K.W. 2015 Fluidic origami with embedded pressure dependent multi-stability: a plant inspired innovation. *J. R. Soc. Interface* **12** (111), 20150639.

LIU, C. & FELTON, S.M. 2018 Transformation dynamics in origami. *Phys. Rev. Lett.* **121** (25), 254101.

LOPEZ, D., ELOY, C., MICHELIN, S. & DE LANGRE, E. 2014 Drag reduction, from bending to pruning. *Europhys. Lett.* **108** (4), 48002.

MARZIN, T., DE LANGRE, E. & RAMANANARIVO, S. 2022 Shape reconfiguration through origami folding sets an upper limit on drag. *Proc. R. Soc.* A **478** (2267), 20220592.

OVERVELDE, J.T.B., DE JONG, T.A., SHEVCHENKO, Y., BECERRA, S.A., WHITESIDES, G.M., WEAVER, J.C., HOBERMAN, C. & BERTOLDI, K. 2016 A three-dimensional actuated origami-inspired transformable metamaterial with multiple degrees of freedom. *Nat. Commun.* **7** (1), 1–8.

OVERVELDE, J.T.B., KLOEK, T., D'HAEN, J.J.A. & BERTOLDI, K. 2015 Amplifying the response of soft actuators by harnessing snap-through instabilities. *Proc. Natl Acad. Sci. USA* **112** (35), 10863–10868.

PERETZ, O., MISHRA, A.K., SHEPHERD, R.F. & GAT, A.D. 2020 Underactuated fluidic control of a continuous multistable membrane. *Proc. Natl Acad. Sci. USA* **117** (10), 5217–5221.

SCHOUVEILER, L. & BOUDAOUD, A. 2006 The rolling up of sheets in a steady flow. *J. Fluid Mech.* **563**, 71.

SCHOUVEILER, L. & ELOY, C. 2013 Flow-induced draping. *Phys. Rev. Lett.* **111** (6), 064301.

SENGUPTA, S. & LI, S. 2018 Harnessing the anisotropic multistability of stacked-origami mechanical metamaterials for effective modulus programming. *J. Intell. Mater. Syst. Struct.* **29** (14), 2933–2945.

SHAN, S., KANG, S.H., RANEY, J.R., WANG, P., FANG, L., CANDIDO, F., LEWIS, J.A. & BERTOLDI, K. 2015 Multistable architected materials for trapping elastic strain energy. *Adv. Mater.* **27** (29), 4296–4301.

SILVERBERG, J.L., EVANS, A.A., MCLEOD, L., HAYWARD, R.C., HULL, T., SANTANGELO, C.D. & COHEN, I. 2014 Using origami design principles to fold reprogrammable mechanical metamaterials. *Science* **345** (6197), 647–650.

TAVAKOL, B., BOZLAR, M., PUNCKT, C., FROEHLICHER, G., STONE, H.A., AKSAY, I.A. & HOLMES, D.P. 2014 Buckling of dielectric elastomeric plates for soft, electrically active microfluidic pumps. *Soft Matt.* **10** (27), 4789–4794.

TREML, B., GILLMAN, A., BUSKOHL, P. & VAIA, R. 2018 Origami mechanologic. *Proc. Natl Acad. Sci. USA* **115** (27), 6916–6921.

VOGEL, S. 1984 Drag and flexibility in sessile organisms. *Am. Zool.* **24** (1), 37–44.

WAITUKAITIS, S., MENAUT, R., CHEN, B.G. & VAN HECKE, M. 2015 Origami multistability: from single vertices to metasheets. *Phys. Rev. Lett.* **114** (5), 055503.

WEI, Z.-B., DAI, X., QUAN, Q. & CAI, K.-Y. 2016 Drogue dynamic model under bow wave in probe-and-drogue refueling. *IEEE Trans. Aerosp. Electron. Syst.* **52** (4), 1728–1742.

VON WIESELSBERGER, C. 1921 Neuere feststellungen under die gesetze des flussigkeits und luftwiderstandes. *Phys.* Z **22**, 321–328.

YASUDA, H., CHEN, Z. & YANG, J. 2016 Multitransformable leaf-out origami with bistable behavior. *J. Mech. Robot.* **8** (3), 031013.

ZHANG, J., CHANGGUO, W.A. & ZHANG, L. 2022 Deployment of SMP Miura-ori sheet and its application: aerodynamic drag and RCS reduction. *Chin. J. Aeronaut.* **35** (8), 121–131.

ZHANG, J., LI, T., WANG, C. & YAN, X. 2021 Aerodynamic drag characteristics of Miura-ori composite structure. *J. Aerosp. Engng* **34** (4), 06021004.

ZULIANI, F., LIU, C., PAIK, J. & FELTON, S.M. 2018 Minimally actuated transformation of origami machines. *IEEE Robot. Autom. Lett.* **3** (3), 1426–1433.